Monthly Notices of the ROYAL ASTRONOMICAL SOCIETY

MNRAS **515,** 4176–4190 (2022)
Advance Access publication 2022 April 9

https://doi.org/10.1093/mnras/stac1172

Intermediate- and high-velocity clouds in the Milky Way – II. Evidence for a Galactic fountain with collimated outflows and diffuse inflows

Antonino Marasco [1]★ Filippo Fraternali,[2] Nicolas Lehner[3] and J. Christopher Howk[3]

[1]*INAF – Osservatorio Astrofisico di Arcetri, Largo E. Fermi 5, I-50127 Firenze, Italy*
[2]*Kapteyn Astronomical Institute, University of Groningen, Postbus 800, NL-9700 AV Groningen, the Netherlands*
[3]*Department of Physics, University of Notre Dame, Notre Dame, IN 46556, USA*

Accepted 2022 April 22. Received 2022 April 22; in original form 2022 February 10

ABSTRACT

We model the kinematics of the high- and intermediate-velocity clouds (HVCs and IVCs) observed in absorption towards a sample of 55 Galactic halo stars with accurate distance measurements. We employ a simple model of a thick disc whose main free parameters are the gas azimuthal, radial, and vertical velocities (v_ϕ, v_R, and v_z), and apply it to the data by fully accounting for the distribution of the observed features in the distance–velocity space. We find that at least two separate components are required to reproduce the data. A scenario where the HVCs and the IVCs are treated as distinct populations provides only a partial description of the data, which suggests that a pure velocity-based separation may give a biased vision of the gas physics at the Milky Way's disc–halo interface. Instead, the data are better described by a combination of an inflow component and an outflow component, both characterized by rotation with v_ϕ comparable to that of the disc and v_z of 50–100 km s^{-1}. Features associated with the inflow appear to be diffused across the sky, while those associated with the outflow are mostly confined within a bicone pointing towards ($l = 220°$, $b = +40°$) and ($l = 40°$, $b = -40°$). Our findings indicate that the lower ($|z| \lesssim 10$ kpc) Galactic halo is populated by a mixture of diffuse inflowing gas and collimated outflowing material, which are likely manifestations of a galaxy-wide gas cycle triggered by stellar feedback, that is, the galactic fountain.

Key words: Galaxy: evolution – Galaxy: halo – Galaxy: kinematics and dynamics – Galaxy: structure.

1 INTRODUCTION

The evolution of late-type galaxies is largely controlled by the cycle of gas between their star-forming disc and their gaseous halo. Galaxies like the Milky Way require a continuous supply of low-metallicity material to replenish the gas used to form stars (Chiappini, Matteucci & Romano 2001; Fraternali & Tomassetti 2012; Saintonge et al. 2013), and most of this gas is expected to originate from smooth accretion from the halo rather than from wet mergers (Sancisi et al. 2008; Di Teodoro & Fraternali 2014). Feedback from star formation and active galactic nuclei is thought to generate galaxy-scale outflows where the gas can, depending on the launching conditions, be expelled beyond the virial radius of the galaxy (Muratov et al. 2015; Mitchell, Schaye & Bower 2020), be dissolved within the low-density circumgalactic medium (CGM; Heitsch & Putman 2009), or return back to the disc in a 'galactic fountain' (GF) cycle (Shapiro & Field 1976; Bregman 1980; Fraternali & Binney 2006). Ultimately, the combinations of inflow and outflow processes regulate the main properties (mass, angular momentum, metallicity) of the galactic interstellar medium (ISM), the reservoir out of which stars form and supermassive black holes feed. An observational strategy to study such processes is to focus on the gas at the interface between the star-forming disc and the halo, which contains information on the combination of all the mechanisms described above. This gas is often referred to as 'extraplanar gas', 'lower' CGM, or, as we prefer to use in this study, 'disc–halo interface' (DHI).

The Milky Way is an optimal laboratory to study the DHI, as our privileged position within the Galaxy offers an almost complete all-sky view of this medium, even though projection effects inevitably complicate our understanding of it (e.g. Zheng et al. 2020). Observational manifestations of ongoing Galactic gas cycle are the so-called high-velocity and intermediate-velocity clouds (HVCs and IVCs; Wakker & van Woerden 1997), spatially extended complexes of neutral and ionized gas with line-of-sight velocities incompatible with them participating in the Galactic rotation. These features have been extensively studied in H I emission (e.g. Wakker 1991; Wakker et al. 2007, 2008; Westmeier 2018) and in absorption of neutral, low- and highly ionized gas towards bright background quasi-stellar objects(QSOs; Sembach et al. 2003; Shull et al. 2009; Ben Bekhti et al. 2012; Lehner et al. 2012; Richter et al. 2017; Clark, Bordoloi & Fox 2021; French et al. 2021) and halo stars (Lehner et al. 2009; Lehner & Howk 2011; Bish et al. 2019; Werk et al. 2019). H I observations have the advantage of providing a uniform coverage across the sky but are sensitive to column densities larger than $\sim 10^{18}$ cm^{-2} (e.g. Lockman et al. 2002). Absorption measurements instead can probe down to much lower hydrogen columns, but only towards a sparse collection of background targets. However, unlike absorption-line studies beyond the Local Group that are typically limited to about one background QSO per galaxy (e.g. Tumlinson et al. 2011; Liang & Chen 2014; Werk et al. 2014, 2016), which makes impossible to characterize individual galaxy haloes in any

★ E-mail: antonino.marasco@inaf.it

details, in the Milky Way, we have the luxury of probing the DHI using several tens of background halo stars with known distance and hundreds of QSOs. This makes the Milky Way an excellent system for studying the DHI with absorption-line observations.

Understanding the nature of the HVCs and IVCs requires the knowledge of three key properties: their distance, metallicity, and three-dimensional (3D) kinematics. Considerable observational efforts have been devoted to determine the former two properties (e.g. Richter et al. 2001; Wakker 2001; Collins, Shull & Giroux 2003; Tripp et al. 2003; Thom et al. 2006, 2008; Wakker et al. 2007, 2008; Zech et al. 2008; Lehner & Howk 2010; Fox et al. 2016). The picture that consistently emerges from these studies is that the IVCs are nearby systems (d < 1–2 kpc) that have near or solar metallicity, while the HVCs are located at larger distances (d < 10–15 kpc)[1] and feature metallicity in the range 0.1–1.0 $Z_{\odot}$. This dichotomy has been traditional interpreted as evidence for a distinct origin for the two cloud populations: internal for the IVCs, and external for the HVCs (with the important exception of the HVCs associated with the Fermi Bubble, see Section 5.3). While the GF is the only plausible internal mechanism that can bring gas at the DHI, several options exist for the external scenario. These include spontaneous condensation of the hot corona as a consequence of thermal instability, an option that is highly debated amongst the theoretical community (e.g. Binney, Nipoti & Fraternali 2009; Nipoti 2010; Sobacchi & Sormani 2019; Sormani & Sobacchi 2019), gas stripped or ejected from satellites (e.g. Bland-Hawthorn et al. 1998; Putman 2006; Olano 2008), fragments of gas filaments accreting from the cosmic web on to the Galaxy (e.g. Kereš et al. 2009; Fernández, Joung & Putman 2012; van de Voort et al. 2019), or gas-rich mini-haloes (e.g. Galyardt & Shelton 2016).

Comparatively, the study of the 3D kinematics of the Galactic DHI has not received the same level of attention. This is surprising, given that the HVCs and IVCs were originally selected on pure kinematic grounds, and kinematics play a crucial role in the interpretation of their origin and in the measurement of their inflow and outflow rates (e.g. Fox et al. 2019; Clark et al. 2021; French et al. 2021). Marasco & Fraternali (2011) were the first to study the global kinematics of the Galactic DHI in the H I phase by applying a parametric model of a thick disc to the data of the LAB survey (Kalberla et al. 2005). They found evidence for a global rotation with a speed comparable to – but slightly lower than – that of the disc, and for an inflow with a velocity of 30–40 km s^{-1}. Similar kinematics are found in the neutral and ionized DHI of external galaxies (Fraternali et al. 2002; Marasco et al. 2019; Li et al. 2021) and in the Milky Way Si IV-bearing gas (Qu et al. 2020). The presence of rotation strongly supported the idea of an internal origin for most of the DHI, but the slower rotation speed and the inflow were not trivial to interpret, plus the model did not reproduce several of the high-velocity H I complexes.

Building on the pioneering works by Fraternali & Binney (2006, 2008), Marasco, Fraternali & Binney (2012) applied a dynamical model of the GF to the same H I data set. In this model, fountain clouds are ejected from the disc by supernova feedback and travel through the halo region before returning back to the Galaxy. Fountain clouds are assumed to be initially ionized, but recombination occurs during their orbit; thus, their neutral phase is observed preferentially in inflow. Also, clouds interact with a pre-existing, slow-rotating, metal-poor hot corona, exchanging momentum with it (which slows their rotation down) and triggering its condensation and subsequent accretion on to the disc (Marinacci et al. 2011; Armillotta et al. 2017). This model reproduces the Galactic H I data remarkably well, explains the origin of the slow rotation and global inflow motion, and predicts an accretion of coronal material on to the disc at a rate similar to the Galactic star formation rate. According to this model, a typical fountain episode produces IVCs that contain only a small percentage (up to 10–15 per cent in mass) of condensed coronal gas. HVCs instead stem from more energetic episodes localized along the Galaxy spiral arms, and can contain a higher percentage of condensed material (about 50 per cent for complex C; Fraternali et al. 2015), which explains the wide metallicity spread centred around sub-solar values that is typically measured in these systems. Thus, in this framework, the properties of the DHI are explained by a combination of internal and external mechanisms, which is in contrast with scenarios where the origin of the HVCs is purely external.

In Lehner et al. (2022, hereafter Paper I of this series), we have built a sample of intermediate- and high-velocity absorption features from the analysis of ultraviolet (UV) spectra of 55 halo stars with high-quality distance measurements. In the current study (Paper II), we make use of simple, parametric models for the gas distribution and kinematics of the Galactic DHI that we constrain using the data set built in Paper I. We show that the resulting kinematics place strong constraints on the origin of the observed features.

This study is structured as follows. In Section 2, we briefly summarize the main results of Paper I and describe the absorption data set that we use in this study. In Section 3, we describe our kinematic models and their application to the data. The main results of our modelling approach are presented in Section 4 and are discussed in the broader context of the origin of the Galactic DHI in Section 5. Conclusions are drawn in Section 6.

In this work, we assume Galactic constants $R_{\odot} = 8.2$ kpc and $v_{\odot} = 232.8$ km s^{-1} (McMillan 2017).

2 DATA SET DESCRIPTION AND BASIC PROPERTIES

We briefly summarize here the main properties of the absorption-line data set built in Paper I, and begin to explore the main structural and kinematic properties of such data. We have targeted a sample of 55 bright (B-type, PAGB/BHB) halo stars at Galactic latitudes $|b| > 15^{\circ}$ using Cosmic Origins Spectrograph (COS) and Space Telescope Imaging Spectrograph (STIS) on board of the *Hubble Space Telescope* (*HST* cycle 17 and 20 programmes – PIDs 11592 and 12982, plus additional archival *HST* data). *HST* spectra cover the wavelength range between 1150 and 1730 Å with a spectral resolution varying between $R \simeq 17\,000$ (for COS) and $R = 45\,800$–$114\,000$ (for STIS), corresponding to a velocity resolution (full width at half-maximum) between 2.6 and 18 km s^{-1}. Using these spectra, we have searched for absorption-line features of intervening gas in the several transitions of atomic and ionic species observable in the wavelength range covered, which includes O I λ1302, C II λ1334, C IV λλ1548, 1550, S II λλ1250, 1253, 1259, Si II λλ1190, 1193, 1260, 1304, 1526, Si III λ1206, Si IV λλ1393, 1402, Al II λ1670, and Fe II λ1608. The rule to claim for a detection is to observe a given feature in at least two different transitions with the same velocity offset. Features are classified as HVCs or IVCs depending on their flux-weighted mean velocity in the local standard of rest (LSR): We take $|v_{\rm LSR}| > 90$ km s^{-1} for the HVCs and $40 \leq |v_{\rm LSR}| \leq 90$ km s^{-1} for the IVCs. The deep, often saturated lines at $|v_{\rm LSR}| < 40$ km s^{-1} are assumed to be due to the Galactic ISM and are excluded from our analysis. Contamination from photospheric stellar lines is a potential issue only for five targets, which are carefully analysed using a

[1] We do not consider the Magellanic Stream in this classification.

combination of stellar templates and H I emission-line spectra to determine the origin of the features observed.

A major improvement with respect to previous studies (Lehner & Howk 2011; Lehner et al. 2012) is the use of *Gaia* EDR3 parallaxes (Gaia Collaboration et al. 2021) to determine directly the distance of most of the target stars in the sample without relying on models of stellar photospheres. In our sample, most distance determinations with *Gaia* EDR3 have an accuracy of about or better than 20 per cent. All the remaining stars but one are associated with globular clusters that have an accuracy on the distance of about 12 per cent. Our sample spans a distance range $1.4 < d < 19.4$ kpc (median d of 6.6 kpc), corresponding to vertical offsets from the Galaxy mid-plane $0.7 < |z| < 14.2$ kpc (median $|z|$ of 4 kpc).

We remark that the resulting data set is not representative for the whole Galaxy halo, but it probes an approximately spherical region of several kpc around the Sun, with the exclusion of the Galactic disc. The limited size of the region probed by our data implies that contamination from the Magellanic Stream is highly unlikely.

2.1 Gas vertical distribution

A key result from Paper I is that the covering factor of target stars that are further away from the Galaxy mid-plane is similar to that determined for distant QSOs, indicating that our sample spans a sufficiently large range in $|z|$ to encompass most of the DHI traced by UV absorption lines. This allows us to determine the scale height of the absorbing gas from the trend of the covering factor with $|z|$.

We determine the vertical distribution of the ionized absorbers in our data set under three assumptions: (a) the ionized material is made by an ensemble of identical clouds; (b) each absorption feature traces one of these clouds; and (c) the covering fraction traced by the most distant target stars ($D \sim 18$ kpc from the Sun) is similar to that of QSOs. Clearly, assumptions (a) and (b) are simplification of the DHI intrinsic properties and must be regarded as working hypothesis, while we know that (c) holds (Paper I).

Under the above assumptions, if a star at a given height z and Galactic latitude b shows $\mathcal{N}$ features, then the cumulative distribution of the ionized material from the mid-plane up to that z will be given by $\mathcal{N} \sin|b|$, where the $\sin|b|$ correction accounts for the projection in the direction perpendicular to the disc. The mean $\langle \mathcal{N} \sin|b| \rangle$ computed over several stars at similar z provides a more precise measurement for this quantity. By applying this procedure to different z bins, we can infer the cumulative cloud number count and fit it with an analytical model for the vertical gas profile.

Here, we make use of an empirical model that has been specifically designed by Oosterloo, Fraternali & Sancisi (2007) to describe the H I vertical distribution of the DHI in the edge-on spiral galaxy NGC 891, and that was later applied to DHI of other galaxies (Marasco et al. 2019; Li et al. 2021), including the Milky Way (Marasco & Fraternali 2011). The model consists of a $\sinh(|z|/h) \times \cosh(|z|/h)^{-2}$ profile, where h is the characteristic scale height. It features a depression for $|z| \to 0$ (so that the DHI 'vanishes' into the ISM), a peak at $|z| \simeq 0.88h$, and an exponential decline at larger heights.

The outcome is illustrated in Fig. 1 (top panel), where we compare the trend of $\langle \mathcal{N} \sin|b| \rangle$ with $|z|$ followed by the data (black points with error bars) with our best-fitting[2] model having $h = 1.4 \pm 0.2$ kpc (solid line, with the surrounding shaded region representing the nominal error on the fit). The bottom panel of Fig. 1 shows this procedure on our sample split between IVCs ($|v_{\rm LSR}| \leq 90\,{\rm km\,s^{-1}}$, green squares) and HVCs ($|v_{\rm LSR}| > 90\,{\rm km\,s^{-1}}$, blue circles), for which we derive scale heights of 1.0 ± 0.3 and 2.8 ± 0.3 kpc, respectively. These values are adopted in our models in Section 3. The recovered scale heights are of course sensitive to the adopted functional form,[3] but quite insensitive on our choice for the binning in z.

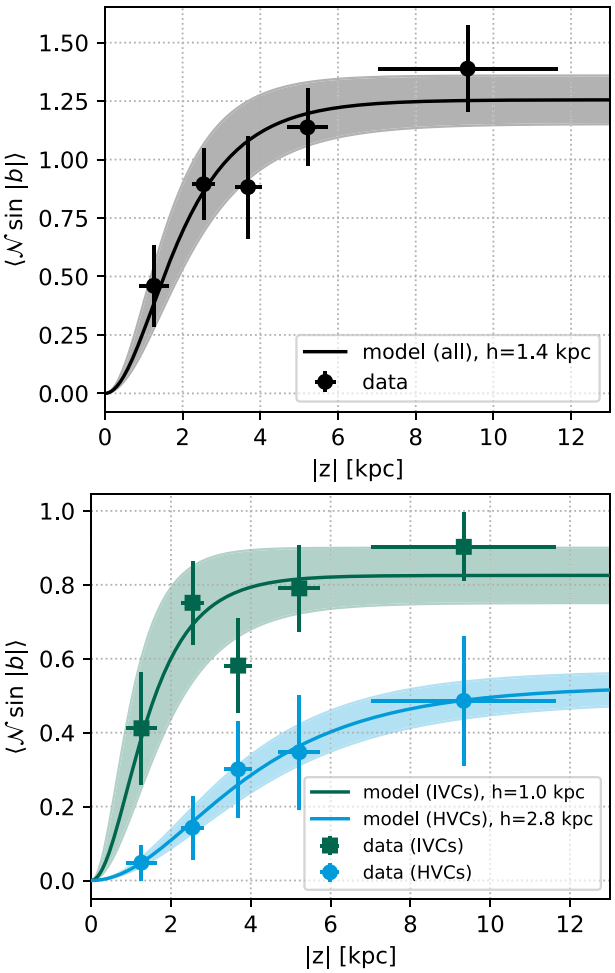

Figure 1. Top panel: mean number of observed absorbing features corrected for projection effects, $\langle \mathcal{N} \sin|b| \rangle$, as a function of $|z|$ (black circles with error bars). The solid lines show the prediction for a density profile $\sinh(|z|/h) \times \cosh(|z|/h)^{-2}$ (see text), where $h = 1.4 \pm 0.2$ kpc, with the grey-shaded region representing the nominal error on the fitted parameters. Bottom panel: as in the top panel, but splitting the sample between IVCs ($|v_{\rm LSR}| \leq 90\,{\rm km\,s^{-1}}$, green squares) and HVCs ($|v_{\rm LSR}| > 90\,{\rm km\,s^{-1}}$, blue circles), for which we find $h = 1.0 \pm 0.3$ and 2.8 ± 0.3 kpc, respectively.

Thus, IVCs are confined within a few kpc from the disc, while HVCs are located at larger distances, which is consistent with the picture shown in H I HVCs and IVCs using the distance bracket method (e.g. Ryans et al. 1997a,b; Wakker & van Woerden 1997; Wakker 2001; Wakker et al. 2007, 2008; Thom et al. 2008). Also, the scale height determined for the whole sample is consistent with that found by Marasco & Fraternali (2011) for the H I phase ($1.6^{+0.6}_{-0.4}$ kpc). We stress that features at $|v_{\rm LSR}| > 170\,{\rm km\,s^{-1}}$ (sometimes referred to

[2]Here, the fitted parameters are h and the normalization of the distribution.

[3]For instance, assuming an exponential profile, we get 3.0 ± 0.6 kpc for the full sample and 2.0 ± 0.7 kpc for the IVCs, but the fit diverges for the HVCs indicating that a different distribution is required to model these data.

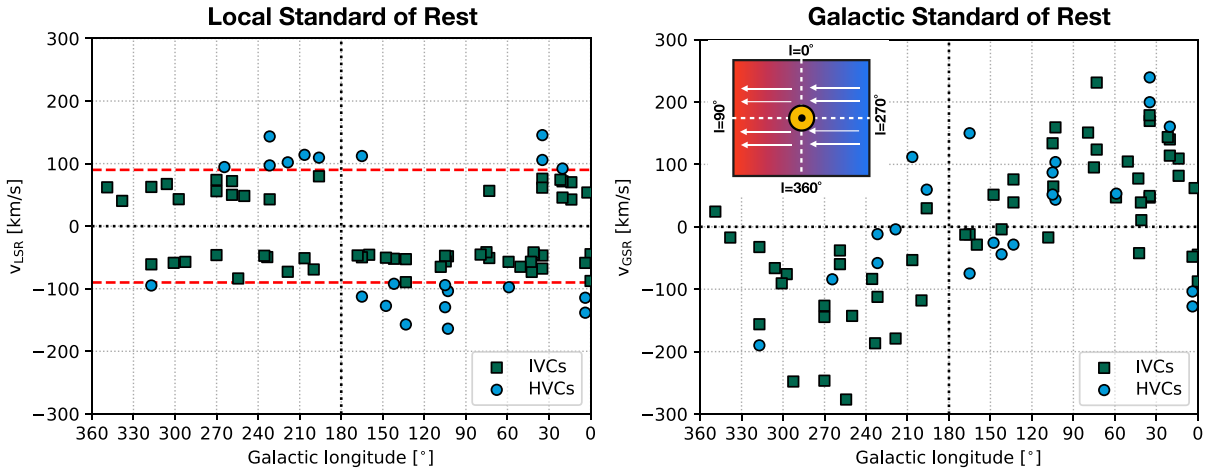

Figure 2. Longitude–velocity diagrams for the absorption features studied in this work. IVCs and HVCs are represented by green squares and blue circles, respectively. The left-hand panel shows velocities in the LSR, where no significant trends with longitude are visible, suggesting the absence of strong peculiar motions in this reference frame. The right-hand panel shows velocities in the GSR. The resulting sinusoidal pattern indicates that the absorbing gas streams along the same direction of the Sun motion, as illustrated in the inset on the top left-hand side. These trends are more defined for the IVCs than for the HVCs. Both panels convey the same message: The dominant motion of the absorbing material is rotation around the Galactic Centre with a speed comparable to that of the disc. The other velocity components appear more substantial for the HVCs than for the IVCs.

as very high-velocity clouds, VHVCs) are not observed in our stellar sample but are routinely detected towards QSOs (e.g. Sembach et al. 2003; Lehner et al. 2012; Richter et al. 2017). This indicates that the VHVC population is located at $|z| \gtrsim 10$ kpc, and is possibly associated with the Magellanic Stream and its Leading Arm (Lehner et al. 2012), or with the outer regions of the Galactic corona (Marasco, Marinacci & Fraternali 2013).

2.2 Basic kinematic properties

While detailed kinematic models are presented in the next section, basic considerations on the main kinematic properties of the absorbers in our sample can be done without recurring to modelling. In Fig. 2, we show the longitude–velocity distribution of the features in our data set. No significant trends are visible when velocities are determined with respect to LSR (left-hand panel of Fig. 2), indicating that the absorbing gas does not have strong peculiar motions in this particular reference frame. Alternatively, this property can be visualized by converting velocities to the Galactic Standard of Rest[4] (GSR), shown by the right-hand panel of Fig. 2: The sinusoidal pattern of the l–v_{GSR} diagram, which features a maximum at $l \simeq 90°$ and a minimum at $l \simeq 270°$, is consistent with the absorbing gas streaming along the same direction of the Sun motion (i.e. towards $l = 90°$), as illustrated in the top left-hand inset of the panel. Both the IVCs and the HVCs seem to participate in this global pattern, although the trend is more defined for the former than for the latter.

These considerations indicate that the absorbing gas rotates in the same direction of the Galaxy, and that such motion is the dominant component of its kinematics (see also Qu et al. 2020). We stress that the change of reference frame from LSR to GSR helps to provide a clearer visualization of this rotating pattern but does not add further information on the 3D kinematics of the gas, which is the subject of the analysis below.

[4]Defined as a reference frame where the Sun is at rest with respect to the Galactic Centre, $v_{GSR} = v_{LSR} + v_{\odot} \sin(l) \cos(b)$

3 KINEMATIC MODELS

Our models stem from those implemented by Marasco et al. (2019, hereafter M19) to describe the morphology and kinematics of the H I in the halo of nearby galaxies from the HALOGAS survey (Heald et al. 2011). Similar models have been used by Marasco & Fraternali (2011) to describe the properties of the H I in the halo of the Milky Way. We briefly summarize here their features, along with the adjustments required to adapt them to the current study.

3.1 Model details

In M19, the gas layer was modelled as an axisymmetric, smooth gas distribution described by four kinematic parameters, namely the gas velocity vector in cylindrical coordinates (v_R, v_ϕ, v_z) plus the gas velocity dispersion σ, and three structural parameters defining the gas radial and vertical distribution. However, due to the intrinsic difficulties in modelling a sparse collection of absorbing features, in this study, we focus solely on the large-scale gas kinematics and fix the gas structure and velocity dispersion as follows.

First, we assume a surface density profile that is constant with radius. This choice is driven by the fact that, since most background sources are high-latitude halo stars with a wide $|z|$ distribution, our data are very informative on the gas profile in the vertical direction but contain little information along the radial direction. We tested this by attempting to fit the data (see Section 3.2) with a more complex model featuring the same parametric surface density profile adopted by M19 (see their equation 1), finding that we could not constrain the parameters describing the surface density. Secondly, we use the characteristic scale height h determined for the DHI in Section 2.1 on the basis of the trend of the covering factor with $|z|$, as discussed in Section 2. This is a necessary assumption given the smooth nature of our DHI model. Finally, we set σ to the value of 20 km s^{-1}. This value is slightly larger than the typical line widths of our absorbing features (10–15 km s^{-1}) but, by visually comparing the model with the data (see Section 4 and Figs 3 and 4), we found it to provide a better description for the velocity spread of our data set. We have verified that assuming a different value of σ has a negligible impact

on our results. This leaves us with three free parameters, which are those describing the velocity vector (v_R, v_ϕ, and v_z).

For any given choice of these three parameters, a Monte Carlo sampling is used to generate the distribution of the ionized gas in the full 6D phase space. An 'internal' projection of such distribution is derived by considering a reference frame located at ($R = R_\odot$, $z = 0$), rotating in the azimuthal direction with a speed equal to $v_\odot$. This frame is used to transform the 6D phase space into a 4D 'observational' space (l, b, v_{LSR}, d), which can be compared with the absorption data as we discuss below. To simplify our notation, in what follows, we refer to the velocity measured in the LSR as v, rather than v_{LSR}.

3.2 Fitting the model to the data

Comparing the smooth, all-sky gas distribution resulting from our model with the discrete absorption-line data set built in this study is not a trivial task. Ideally, for any given sightline probed by a background star, one would derive model absorption-line profiles of the various ionized species observed for comparison with the data. This would demand detailed knowledge of both the physical conditions of the gas and the ionizing radiation field, which clearly are not readily available. In this study, instead, we adopt a simplified, purely kinematic approach based on the philosophy that the optimal model is the one that best reproduces the distribution of the absorbers in the observed (l, b, v, d) space. To pursue this approach, we first need to build the observed and predicted distributions, and then to define the method to compare them.

We focus first on our model. For each target halo star (table 1 in Paper I), we produce a synthetic light-cone by considering all Monte Carlo sampler (or 'clouds') within a fixed aperture δ from the (l, b) sightline of the star. These clouds are used to build a smooth probability distribution in the (v, d) space relative to that particular sightline. In principle, δ should sample an angle similar to the background stars' angular size (microarcsecond scales), but values up to $\sim 8^\circ$ have a negligible impact on our results and provide a better sampling of the probability distribution for a fixed number of clouds N_{cl}. After experimenting with different values of N_{cl} and δ, we found that $N_{cl} = 2.5 \times 10^6$ and $\delta = 4^\circ$ give the optimal compromise between model accuracy and computational speed. We stress that these N_{cl} samplers are by no means representative of realistic clouds in the Galactic halo, but are simply used as a convenient way to sample a continuous gas distribution. Examples of model probability distribution associated with the various sightlines are shown in Figs 3 and 4 as solid lines. Such distributions will depend on the model parameters: For instance, larger scale heights will stretch them towards higher d, while negative v_z will shift them towards more negative v (especially for high-latitude sightlines), and so on.

We must now build the corresponding distribution for the data. Unfortunately, the data do not fully sample the (v, d) space but provide only discrete sampling in the velocity direction, corresponding to the v_{LSR} entries reported in table 2 of Paper I. We therefore approximate the distribution in the v direction by considering a triangular function that starts from (and ends at) zero at velocities equal to v_1 and v_2 (as reported in table 2 of Paper I), and reaches a maximum at the observed v_{LSR}. This approach is an optimal compromise between model accuracy and computational speed: It is more realistic than adopting a flat probability distribution between v_1 and v_2 (corresponding to flat velocity profiles for the absorption features, which are never observed), and faster to compute than the 'correct' distribution corresponding to the observed absorption velocity profiles, which have complex shapes and depend on the atomic species considered. We assume a constant probability distribution in the d direction for $d < d_\star$ ($d_\star$ being the distance of the background star), with a decline at larger d following a Gaussian distribution with standard deviation given by the uncertainty on $d_\star$. We normalize the distribution associated with each feature by setting to one the probability integrated in the (v, d) space. In Figs 3 and 4, the observed probability distributions are shown as shaded horizontal stripes.

A 'likelihood' estimator $\mathcal{L}$ can be determined by multiplying the probability distribution of the model by that of the data. With our implementation, this can be conveniently computed as

$$\mathcal{L} \propto \frac{1}{n_{tot}} \sum_{i=1}^{N_\star} \left(\sum_{n=1}^{n_{cl}} \mathcal{P}_i(v_n, d_n) \right), \quad (1)$$

where n_{tot} is the total number of clouds, the external sum is extended to all $N_\star$ sightlines, the internal sum is extended to all n_{cl} clouds along a given sightline i, and $\mathcal{P}_i(v_n, d_n)$ is the observed probability density for sightline i computed at the (v_n, d_n) location of cloud n. In practice, equation (1) defines $\mathcal{L}$ as proportional to the sum of the observed probability density sampled at all the (v, d) locations of the model clouds, which mathematically corresponds to multiplying the observed and the predicted probability distributions, as requested. The value of $\mathcal{L}$ will increase (decrease) when more (less) clouds fall within (v, d) regions compatible with our data, while the n_{tot} normalization factor in equation (1) ensures that $\mathcal{L}$ does not depend on the total number of clouds used to build our model.

In our computation of n_{tot}, we do not account for clouds located in 'forbidden' regions of the (v, d) space that cannot be probed by the observations. Specifically, we exclude clouds with $|v| < 40\,\mathrm{km\,s^{-1}}$, as this velocity regime is systematically occupied by material in the Galaxy disc,[5] along with clouds at distances beyond those of the target stars (plus the distance error) and those falling in (v, d) regions associated with features contaminated by stars ($f_\star = 1$ in table 2 of Paper I). Sightlines with non-detections are included in the analysis since, even though they do not contribute to increase the probability sums in equation (1) (since $\mathcal{P}_i = 0$ everywhere), they affect the value of n_{tot} if clouds are present along those directions.

To determine the optimal model parameters, the likelihood is multiplied by an uninformative (flat) prior to give the posterior probability distribution, which is sampled with an affine-invariant Markov chain Monte Carlo (MCMC) method using the PYTHON implementation by Foreman-Mackey et al. (2013). The MCMC method allows us to fully sample the parameter space in order to account for possible degeneracies, which may be expected given the limitations of our data set. We stress that, while the expression defined in equation (1) is a reasonable 'figure-of-merit' function to compare the model with the data, it is extremely hard to robustly quantify the uncertainties associated with our modelling. This is primarily due to the intrinsic differences between the model, which represents a smooth and axisymmetric distribution of gas, and the observations, which are a sparse collection of absorption-line measurements. We therefore expect our MCMC routine to capture the overall shape of the posterior distribution, but to be agnostic on its width, which implies that the estimated uncertainties on the model parameters must be considered with caution.

[5]The velocity range occupied by the disc varies with l and b, but the adopted constant velocity cut is a very good approximation for $|b| > 30^\circ$.

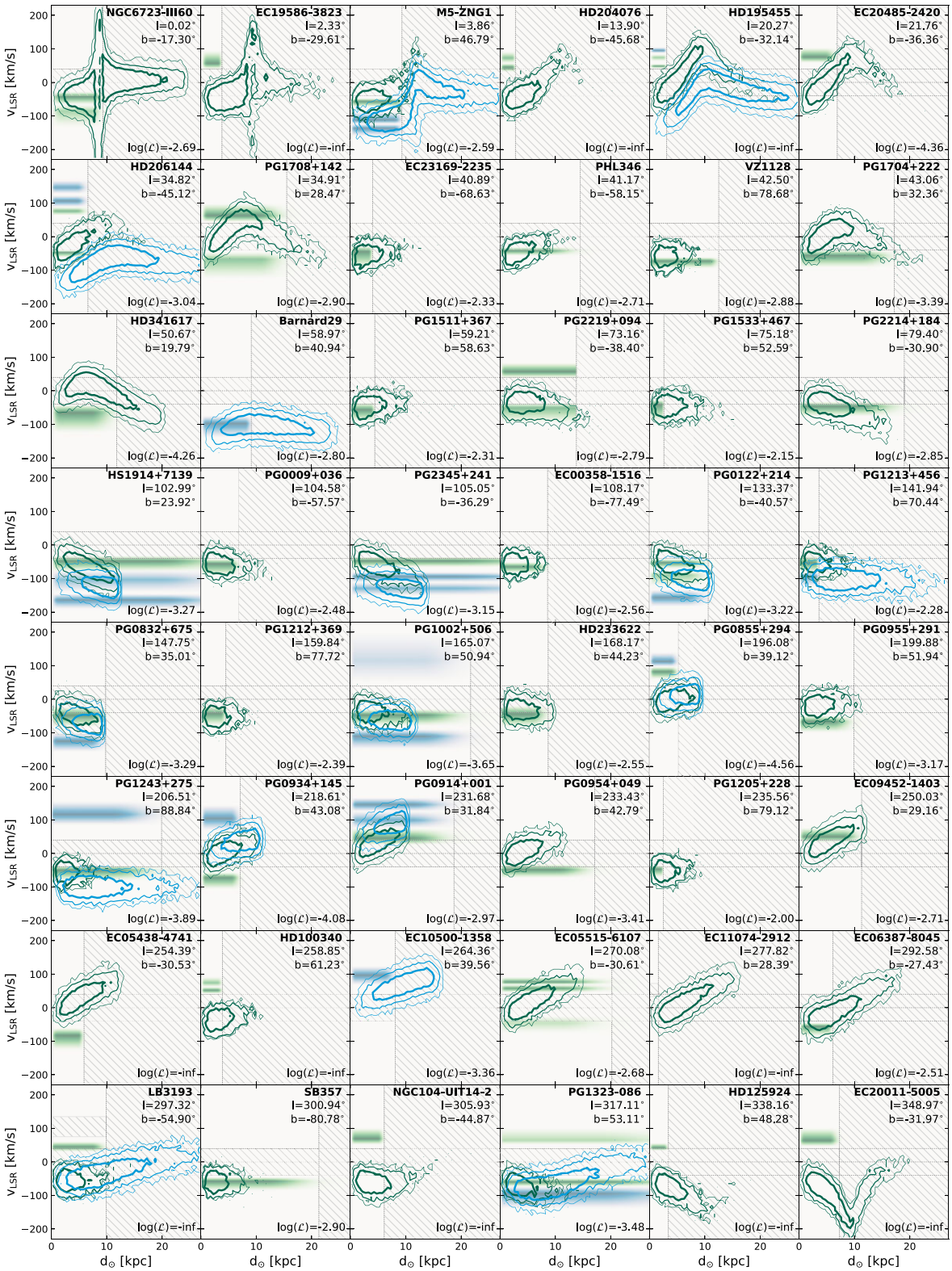

Figure 3. Comparison between the kinematics of the ionized absorbers around the Milky Way and those predicted by our two-component (IVCs + HVCs) model. Each panel shows the (v, d) probability distribution towards a given target star, indicated in the top right-hand corner. The data are shown as shaded horizontal stripes (in green for the IVCs, in blue for the HVCs), with thicknesses corresponding to the velocity widths of the absorption features. Our best-fitting models are shown with green (IVCs) and blue (HVCs) contours, representing the 68 per cent, 95 per cent, and 99.7 per cent of the enclosed probability. The hatched areas highlight regions at distances or velocities that cannot be probed by the observations. Partial likelihoods associated with each sightline are reported in the bottom right-hand corner of each panel, with '-inf' flagging the cases where there is zero overlap between the model and the data ($\mathcal{L} = 0$).

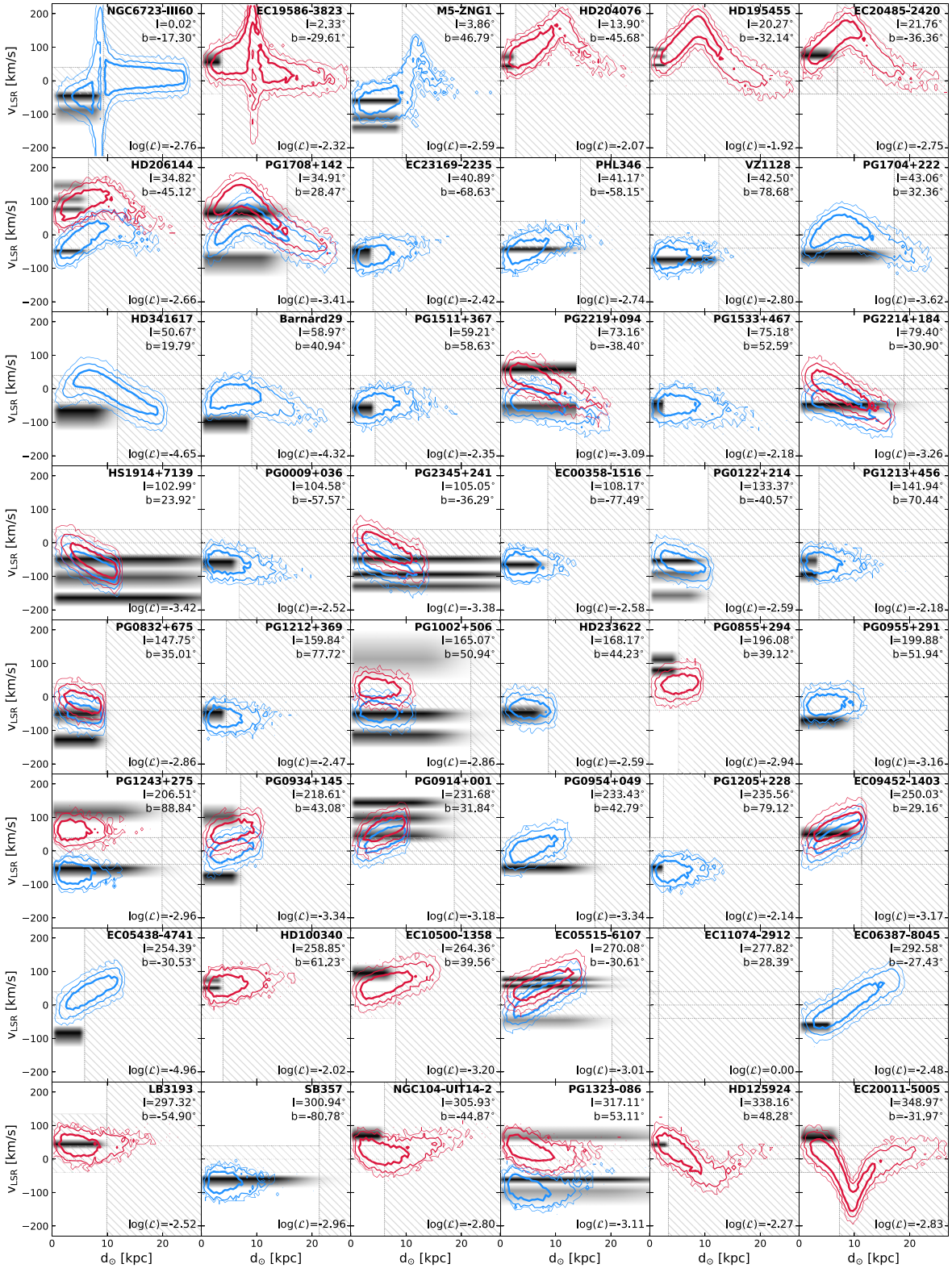

Figure 4. Comparison between the kinematics of the ionized absorbers around the Milky Way and those predicted by our two-component (inflow + outflow) model. Each panel shows the (v, d) probability distribution towards a given target star, indicated in the top right-hand corner. The data are shown as shaded horizontal stripes, with thicknesses corresponding to the velocity widths of the absorption features. Our best-fitting models are shown with blue (inflow) and red (outflow) contours, representing the 68 per cent, 95 per cent, and 99.7 per cent of the enclosed probability. The hatched areas highlight regions at distances or velocities that cannot be probed by the observations. Partial likelihoods associated with each sightline are reported in the bottom right-hand corner of each panel.

Table 1. Best-fitting parameters for our two-component models of ionized gas in the Galactic halo. The model likelihoods are reported in the last row.

Parameter	Scenario 1		Scenario 2	
	IVCs ($\mathrm{km\,s^{-1}}$)	HVCs ($\mathrm{km\,s^{-1}}$)	Inflow ($\mathrm{km\,s^{-1}}$)	Outflow ($\mathrm{km\,s^{-1}}$)
v_ϕ	224 ± 19	143^{+67}_{-33}	233 ± 18	232^{+91}_{-54}
v_z	-57^{+18}_{-13}	-102^{+33}_{-59}	-67^{+8}_{-11}	62^{+55}_{-40}
v_R	25^{+15}_{-20}	63^{+45}_{-53}	30^{+15}_{-11}	-22^{+39}_{-35}
$\log \mathcal{L}$	-3.02		-1.44	

4 RESULTS OF THE MODELS

We run our MCMC routine using 64 walkers and chains of 2000 steps. After visual inspection of the chains, we decided to discard the initial 500 'burn-in' steps beyond which the chains stabilize, and proceeded to inspect the posterior probability distributions. We found the posterior to be multimodal, featuring three separate peaks in the (v_R, v_ϕ, v_z) parameter space. This indicates that a single-component model provides a poor representation of our data, and that a more complex, multicomponent model is required to fully account for the data complexity. We investigate this further below, exploring two different scenarios.

4.1 Scenario 1 – IVCs and HVCs

In this scenario, we consider the IVCs ($|v| \leq 90\,\mathrm{km\,s^{-1}}$) and the HVCs ($|v| > 90\,\mathrm{km\,s^{-1}}$) as separate populations, each described by its own scale height (fixed to 1.0 kpc for the IVCs and to 2.8 kpc for the HVCs, see Section 2.1) and kinematics. We stress that this is a somewhat phenomenological separation, based on the classical distinction between the HVCs and IVCs, and makes no assumption on the physical origin of these two populations.

We fit each population separately, finding a well-defined posterior distribution for the IVCs and a double-peaked posterior distribution for the HVCs. These are shown in the top panels of Fig. B1. We take the median of such distributions as best-fitting values, and compute the error bars as half the difference between the 84th and 16th percentiles. The parameters derived, reported in the third and fourth columns of Table 1, indicate that the IVC population is characterized by fast rotation velocities (compatible with $v_\odot$) and an inflow speed of $\sim 60\,\mathrm{km\,s^{-1}}$, whereas the HVC population rotates slower (120–200 $\mathrm{km\,s^{-1}}$) and accretes at a faster pace ($\sim 100\,\mathrm{km\,s^{-1}}$). We get positive v_R for both components, but with uncertainties that are compatible with 0. Interestingly, the different inflow velocities are compatible with a scenario where the HVCs 'rain down' from the CGM and get decelerated in the process by interaction with the hot corona, finally appearing as IVCs when they approach the Galactic disc. This would also explain the different scale heights found for the two populations. We notice that, in spite of the fact that IVCs and (in particular) HVCs were originally selected as clouds whose v deviates from the predictions of a rotating thin disc model (e.g. Wakker 1991), we derive substantially large rotational velocities for both populations. This result is not controversial given that rotating clouds in the halo can feature $|v| > 90$–$100\,\mathrm{km\,s^{-1}}$ if they are located at large distances from the Galactic Centre, as we show in Appendix A.

Our best-fitting model and our data set are compared to each other in Fig. 3 that shows, for all the sightlines that feature at least one detection, the probability distribution of the model (green and blue contours for the IVC and HVC component, respectively) and of the data (green-shaded and blue-shaded horizontal stripes for the IVCs and HVCs, respectively) in the (v, d) space. The IVC (HVC) model is shown only if IVC (HVC) features are detected along a given sightline. Clearly, our model seems to be compatible with the v–d distribution of the absorption features observed towards several target stars. However, there are some sightlines where it predicts velocities that have opposite signs compared to the data (EC19586-3823, HD204076, HD195455, EC20485-2420, HD206144, PG1243 + 275, HD100340, NGC 104-UIT14-2, HD125924, EC20011-5005). In particular, it fails to reproduce many of the features observed at positive v (see, for instance, the third-to-sixth panels in the top row of Fig. 3, or the first panel in the second row). This suggests that a scenario where the IVCs and HVCs are treated as separate components, each described by its own simple kinematics, is not fully adequate to describe the observed data set.

4.2 Scenario 2 – inflow and outflow

In the second scenario, we adopt a more physically motivated distinction and model the DHI as a combination of an outflow component ($v_z > 0$), representing material ejected from the Galactic disc by stellar feedback, and an inflow component ($v_z < 0$) either due to the previously ejected material returning back to the disc or to new gas that joins the Galaxy for the first time. This approach adds further complexity, as we do not know a priori which absorption feature is associated with which component. Our strategy is to fit both components at the same time, assigning each sightline to one component or the other depending on which provides the highest 'local' likelihood, given by the term in parentheses in equation (1). We further consider the possibility that both components are visible along a given sightline, which we adopt when the local likelihood of the combined inflow + outflow model is larger than $f \times$ the highest single-component likelihood. We set f to 1.2 (i.e. we require a 20 per cent better likelihood to accept both components at the same time), which we found to optimally capture the few occurrences of this situation. With this approach, the assignment of a given sightline to either component (or to both components simultaneously) will vary depending on the model parameters, which are fitted to the data. For simplicity, we fix the scale height of both components to the value of 1.4 kpc, representative for the whole ionized gas layer as discussed in Section 2.1.

The best-fitting parameters obtained for this scenario are listed in the rightmost two columns of Table 1. Here, the ionized gas is best described by two rapidly rotating ($v_\phi \sim v_\odot$) gas layers, one inflowing and the other outflowing at about the same speed ($\sim 65\,\mathrm{km\,s^{-1}}$). As in the previous scenario, also in this case radial motions are present, but are small ($\sim 30\,\mathrm{km\,s^{-1}}$) for the inflow component and compatible with zero for the outflow component. With respect to the inflow, the parameters of the outflow are characterized by large uncertainties, which are mainly caused by the posteriors of v_ϕ, v_z, and v_R being positively correlated, as shown in the bottom panels of Fig. B1.

This model and the data are visually compared in Fig. 4 using the (v, d) diagrams, as in the previous case. This scenario appears to be better suited to reproduce the kinematics of the absorbers: With the possible exception of EC05438-4741, there are no sightlines where the model and the data have opposite velocity signs, and virtually all features show some degree of overlap with at least one of the two components in the (v, d) space. More quantitatively, this scenario provides a much higher (about 1.6 dex) likelihood compared to the previous case, as reported in the last row of Table 1.

We have also attempted a sightline-by-sightline comparison between the two models by limiting the computation of equation (1) to individual target stars. This provides 'partial' likelihoods that are

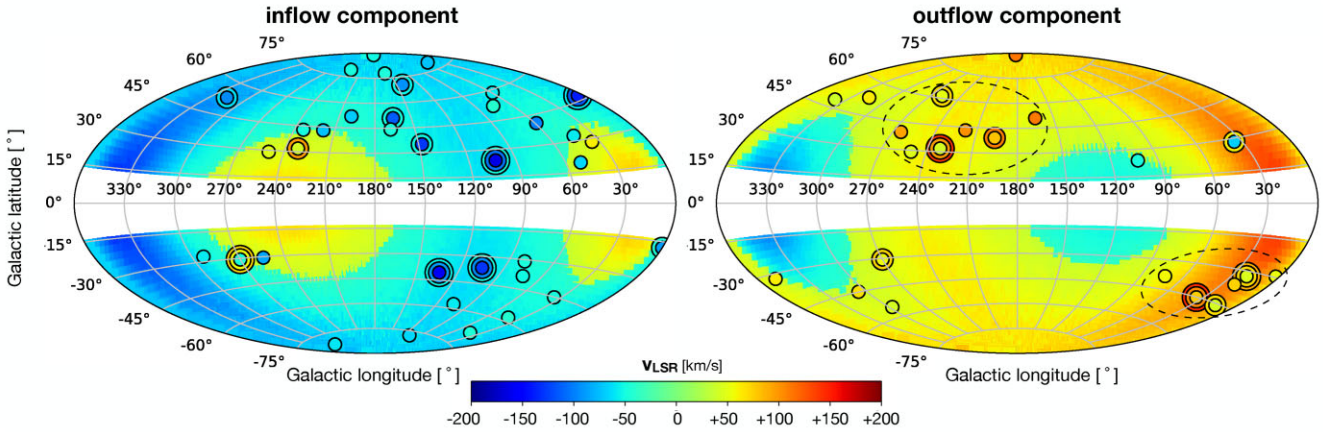

Figure 5. Comparison between the all-sky velocity fields predicted by our best-fitting inflow + outflow models (background colours) and the LSR velocity of the observed absorption features (coloured circles). Concentric circles are used when multiple detections are found towards the same target star. The map on the left-hand side (right-hand side) shows the 52 (33) absorbers compatible with the inflow (outflow) component. The dashed ellipses mark the locations of the biconic outflow encompassing most of the observed feature associated with the outflow component.

informative of how well our model performs on that particular line of sight, being agnostic of the other targets. These partial likelihoods are reported in the bottom right-hand corner of the various panels in Figs 3 and 4. Comparing these numbers reveals that, out of the 47 sightlines with at least one detection, 23 have similar (within a factor of 2) likelihood in both scenarios, 6 have a higher likelihood in scenario 1, and 18 have a higher likelihood in scenario 2. This analysis confirms that the latter scenario provides a better description of our data, both as a whole and for most individual sightlines.

We now turn our attention to the distinction between inflow and outflow. Using an approach similar to that adopted above to compute partial likelihoods, we find that 45 features (58 per cent) are better described by the inflow component, 26 (33 per cent) by the outflow, while 7 (9 per cent) are similarly well described by both components. The highest number of features reproduced by the inflow can be interpreted as different covering fractions associated with the two components: that is, the inflowing gas is more diffuse, whereas the outflowing material is more clumpy and/or collimated. This can be better appreciated in Fig. 5, which shows the all-sky moment-1 map[6] predicted by our inflow (on the left-hand side) and outflow (on the right-hand side) model, overlaid by the absorption features associated with each component. We stress that this visualization is less informative than the (v, d) diagrams of Fig. 4, since it misses the information along the line of sight. However, it helps in revealing that the majority (70 per cent) of the features associated with the outflow occupy two well-defined regions in the sky (dashed ellipses in Fig. 5). Such regions have approximately the same $|b|$ (but with opposite sign) and are separated by $\Delta l \simeq 180^\circ$, suggesting the presence of a biconic outflow driven by star formation in the vicinity of the Sun. We discuss this structure further in Section 5.3.

5 DISCUSSION

5.1 HVCs, IVCs, and the GF

The results of the previous section indicate that the observed absorption features are well described by two gaseous components, both rotating with a speed similar to that of the Galactic disc, accreting on to or escaping from the Galaxy with vertical speeds of several tens of $\mathrm{km\,s^{-1}}$. The dominant kinematics of either component is the rotation at $v_\phi \sim v_\odot$, indicating that both components are 'aware' of the presence of the disc and, possibly, are causally related to it. Radial motions, if present, are limited to a few tens of $\mathrm{km\,s^{-1}}$ (for the inflow) or are affected by large uncertainty (for the outflow).

A promising physical mechanism that can explain such kinematics is that of the GF (e.g. Shapiro & Field 1976; Bregman 1980; Fraternali & Binney 2006), where gas is expelled from star-forming regions by stellar feedback and travels through the lower regions of the halo before making its return to the disc. Accepting this mechanism as the origin of the observed features implies that not only the IVCs, but also several HVCs are produced by feedback from star formation. This appears to be in tension with the different distance, metallicity, and dust content measured for these systems, with the HVCs being typically more metal- and dust-poor and being located at larger distances from the disc than the IVCs (Savage & Sembach 1996; Richter et al. 2001; Wakker 2001, 2004; Tripp et al. 2003). On the other hand, both the IVCs and the HVCs share the same column density distribution function (French et al. 2021), which can be interpreted as due to a common physical mechanism that shapes the two cloud populations.

We now discuss how a revision of the standard fountain model, described in detail by Fraternali (2017), can account for these inconsistencies. In this revised GF framework, metal-rich clouds launched from the galactic disc mix with the metal-poor coronal gas pre-existing in the halo, triggering the condensation of the latter on to the turbulent wakes that form behind the clouds mostly due to the Kelvin–Helmholtz instability (see also Marinacci et al. 2011; Armillotta et al. 2017; Kooij, Grønnow & Fraternali 2021). This interaction produces a complex, multiphase gaseous structure that, with time, becomes progressively more diluted by coronal gas, and therefore less metal- and dust-rich. The condensed coronal gas eventually precipitates on to the disc supplying new fuel for future star formation. The contamination of coronal gas is minimal for short orbital times, corresponding to moderate ejection speed from the disc (in the range 50–100 $\mathrm{km\,s^{-1}}$, which provides an excellent description for the properties of the IVC population; see Marasco et al. 2012), but can become the dominant component for longer trajectories/high-speed ejections. Fraternali et al. (2015) applied this

[6]Derived in our model by excluding gas at $|v| < 40\,\mathrm{km\,s^{-1}}$ and $d > 7\,\mathrm{kpc}$, corresponding to the median d of our target star sample.

GF model to the specific case of the HVC complex C finding that, for an ejection speed of $\approx 210\,\mathrm{km\,s^{-1}}$ from the outer regions of the Cygnus spiral arm, the model did not only reproduce the distance, structure, and kinematics of this complex, but also its metal content and the metallicity trend with H I column density. Similar models were also successfully applied to the Smith Cloud (Smith 1963) by Marasco & Fraternali (2017).

The above results, together with those obtained in the current study, suggest a scenario where the IVCs originate from less powerful but more frequent feedback episodes that produce a large population of disc-like metallicity halo clouds, while the HVCs are produced by rarer, more powerful ejections that give rise to large gas complexes whose mass is largely contaminated (~ 50 per cent in the case of complex C) by condensed coronal material. Hence, distances, metal, and dust content of the clouds populating the DHI are a direct consequence of the ejection speed from the disc. Interestingly, while the simple models used in this work cannot fully capture the complexity of the GF dynamics, the large uncertainties associated with the parameters of outflow component in Table 1 can be interpreted as due to the existence of a wide distribution of outflow velocities, which are expected by theoretical models of stellar feedback, rather than to a unique value of v_z. Future studies could investigate the relation between the orbital time of individual clouds and metallicity.

Another argument against a GF origin is given by the excess of features associated with the negative v_z component, which is not trivial to interpret. GF models applied to the whole H I DHI of the Milky Way indicate that the outflowing leg of the fountain must be largely ionized (Marasco et al. 2012); thus, one would expect the majority of the ionized absorbers to be compatible with a model with positive v_z. Instead, out of 78 detections, only a number between 26 and 33 (33 per cent–42 per cent) are compatible with an outflow. Similar evidence for prevalent inflow has been found by Bish et al. (2019) by studying the ionized gas absorption features in the spectra of 54 high-latitude ($|b| > 60^\circ$) blue horizontal branch stars in the Galaxy halo, and by Clark et al. (2021) (but see Section 5.2). Also, the Milky Way is not the only galaxy where the ionized DHI is seen preferentially in accretion. The extraplanar Hα-emitting gas of the nearby galaxy NGC 2403 appears to be globally inflowing on to the disc, like its H I counterpart (Fraternali, Oosterloo & Sancisi 2004). Zheng et al. (2017) studied the DHI of M33 in absorption towards seven UV-bright stars evenly distributed across the galaxy disc, finding evidence for a widespread inflow. Li et al. (2021) modelled the Hα emission-line cube of NGC 3982 and NGC 4152, two nearby star-forming galaxies, finding that the ionized DHI of these systems, as a whole, is better reproduced by an inflow, rather than by an outflow.

However, our findings of Section 4 provide a solid counterargument, based on the variation of the filling factor: The more diffuse (large filling factor) inflow component is easier to detect than the more collimated (small filling factor) outflowing gas. This would explain not only why inflow features are more routinely observed, but also the results of Li et al. (2021) based on spatially resolved Hα emission-line observations, as an inflow model will be typically preferred when the data are described with a single component. Our argument is supported by the recent hydrodynamical model of stellar feedback developed by Kim & Ostriker (2018), who found that the warm gas is mostly confined in small cloudlets during the outflow-dominated phase of the fountain, but becomes the main volume-filling component during the inflow-dominated phase (see their fig. 2). Also, dedicated hydrodynamical simulations of cloud–corona interaction (Marinacci et al. 2011; Armillotta et al. 2017) have shown that most of the volume is filled by low-column-density gas at temperatures of 10^5–10^6 K (typical of the low-ionized species studied in this work) located in the turbulent wake trailing the cloud. Since the wake grows with time, the covering factor of this component is larger during the descending (inflowing) part of the cloud orbits. Interestingly, these simulations also show that cold gas at column densities typical of the H I complexes observed in emission is confined to the fountain front and to a few high-density 'knots' within the wake; thus, its covering fraction is always lower than that of the warm/ionized material, in qualitative agreement with the observations (e.g. Lehner et al. 2012; Westmeier 2018).

A possible complication to this picture is given by the fact that outflows are more routinely observed than inflows in down-the-barrel studies of star-forming galaxies at intermediate redshift (e.g. Rubin et al. 2014). However, down-the-barrel measurements are mainly sensitive to gas in front of UV-bright star-forming regions of the disc, where outflows are presumably more frequent, and may miss any intervening component that is more sparsely distributed over the whole galaxy area. This limitation is not present in our work or in emission-line studies like that of Li et al. (2021), which are not biased towards regions with high star formation rates.

In the light of these considerations, we argue that our data are largely consistent with a GF scenario where the fountain material is ejected from the disc in collimated structures and returns back as a more diffuse, volume-filling 'rain'. In this picture, both the IVCs and (most of) the HVCs originate from stellar feedback, but develop distinct physical properties due to a diverse level of interaction between the fountain clouds and the pre-existing hot circumgalactic gas.

5.2 Do HVCs and IVCs trace gas accretion on to the Galaxy?

Star-forming galaxies have required throughout cosmic time a continuous supply of gas to replenish the material used for their star formation (e.g. Pezzulli & Fraternali 2016; Schönrich & McMillan 2017). In the local Universe, accretion provided by wet mergers accounts at most by one-fifth of the galaxy star formation rates (Sancisi et al. 2008; Di Teodoro & Fraternali 2014); thus, most gas accretion must come directly from cold filaments or from the cooling of the hot CGM (e.g. Kereš et al. 2005; Dekel & Birnboim 2006). A key question to address is whether some of the ionized features studied in this work are associated with a population of accreting extragalactic clouds, which can potentially refuel the Galaxy at the rate required. To fully address this question, one would need to know not only the 3D kinematics of the ionized material, but also the hydrogen masses (or column densities) of each absorption feature. This would require detailed photoionization modelling, which goes beyond the scope of this work. None the less, qualitative considerations can be done.

Recently, Fox et al. (2019) used the UV metal-line absorption data set of QSOs built from the COS archive by Richter et al. (2017) to determine the rates of gas flow around the Galaxy. They found evidence for both inflow and outflow, as expected from an ongoing GF cycle, and measured an inflow rate larger than the outflow rate, which they took as evidence for gas accretion on to the Galaxy. Clark et al. (2021) used stacked spectra to infer the spatial distribution of the inflow and outflow features, finding that the former were confined to small, well-defined structures, while the latter were spread more uniformly across the sky, which is the opposite of what we find here. There are three main differences between this study and the works of Fox et al. (2019) and Clark et al. (2021). The first is that they focus on the $|v_{\mathrm{LSR}}| > 90\,\mathrm{km\,s^{-1}}$ velocity range; thus, IVCs – which are dominant in our data set – are excluded from their analysis.

Secondly, they use QSOs instead of stars, which probe not only the HVCs, but also the VHVC population, which is not observed towards halo stars and is likely to have a distinct origin (Paper I). The third difference is that, in their works, inflow and outflow features are separated on the basis of the sign of $v_{\rm GSR}$, rather than using kinematic models as we do in our study. We caution that this approach may lead to spurious results in a scenario where clouds at the DHI have complex kinematics and a wide range of distances from the Sun. Such approach certainly cannot be applied to our data set: As shown by the right-hand panel of Fig. 2, adopting the $v_{\rm GSR}$-based separation would result in having half of the sky – the half that the Sun is approaching due to its rotation around the Milky Way centre – populated by outflowing gas, and the other half populated by inflowing gas, which would appear quite unrealistic.

In general, we cannot rule out that some of the features in our data set are associated with genuine extragalactic gas accretion, but the results of Section 4 indicate that the bulk of the IVC and HVC population do not originate from a continuous rain of material from outside the Galaxy. Instead, as discussed above, IVCs and HVCs appear to be manifestations, at different $v_{\rm LSR}$, of the gas cycle occurring at the disc–corona interface triggered by stellar feedback.

Accretion of condensed coronal gas on to the disc is one of the key ingredients of the GF model of Fraternali (2017). Signature of this process ongoing is the variation of the cloud kinematics due to the interaction with coronal gas: Momentum exchange between the two components slows down the cloud rotation[7] and makes them acquire a radially inward motion. At a fixed coronal rotation speed, the magnitude of these effects depends solely on the efficiency of the coronal gas condensation, which therefore can be inferred by applying a dynamical model of the GF to high-quality DHI data. Marasco et al. (2012) applied this model to the all-sky H I data of the Milky Way and found that, for a coronal gas accretion rate similar to the Galactic star formation rate, it provided an excellent description of the H I data set. Marasco et al. (2013) showed that the same model reproduced also the global kinematic trend of the ionized gas absorbers observed towards QSOs and towards the small sample of stellar targets available at that time.

While the ascending and descending v_z inferred for our data set are similar to those derived for the Milky Way and for external galaxies by GF models, the kinematic signatures expected in the case of interaction with the corona (decreased v_ϕ and negative $v_{\rm R}$ for the descending phase) do not seem to be evident. Taken at face value, the positive $v_{\rm R}$ found for the inflow component and the v_ϕ that closely matches that of the disc suggest that the cloud–corona interaction is very limited or does not occur at all. Unfortunately, as discussed in Section 4, it is difficult to determine the error bars associated with our model parameters. Lowering the value of v_ϕ by 10–20 km s^{-1} and that of $v_{\rm R}$ by ∼30–40 km s^{-1} gives a model that is slightly worse than that shown in Fig. 4, but still provides a good description of the absorption feature kinematics. Our conclusion is that, with only the data set analysed in this study, it is not possible to robustly assess the magnitude of the interaction between the fountain clouds and the CGM.

Finally, we remark that cold-mode accretion occurring at the periphery of the disc (e.g. Trapp et al. 2022) may be another viable gas accretion channel, though virtually impossible to test with the available data set given the lack of low-latitude target stars.

[7]Because coronal gas is expected to rotate slower than the ISM on both observational (Hodges-Kluck, Miller & Bregman 2016) and theoretical (Marinacci et al. 2011; Pezzulli, Fraternali & Binney 2017) grounds.

5.3 Biconic outflow and nuclear activity

Biconic outflows of ionized gas are routinely observed at the centre of starbursts or in galaxies hosting AGN, but with speeds that can reach thousands of km s^{-1} (e.g. Veilleux, Cecil & Bland-Hawthorn 2005; Fiore et al. 2017). The Milky Way, with its Fermi Bubble (Su, Slatyer & Finkbeiner 2010), is no exception: A Galactic wind – possibly associated with the past activity of its supermassive black hole Sgr A* – is seen in different gas phases ranging from the hot and highly ionized (Kataoka et al. 2013; Ponti et al. 2019) to the the warm ionized (Fox et al. 2015; Bordoloi et al. 2017), cold atomic (McClure-Griffiths et al. 2013; Di Teodoro et al. 2018), and molecular (Di Teodoro et al. 2020) phase.

We argue that the biconic outflow feature discussed in Section 4.2 is not associated with the Fermi Bubble, for various reasons. Fig. 5 shows that only the absorbers at $b < 0°$ cluster close to $l \sim 0°$, while those at $b > 0°$ are closer to the anti-Centre. While this implies a geometry that is inconsistent with that expected from a nuclear wind, one may argue that the northern and the southern structures of the bicone are uncorrelated, with only the latter being associated with the Fermi Bubble. However, most the target stars in the southern region have distances from the Sun in the range 3–4.6 kpc. Considering that these are upper limits to the actual distance of the absorbing material, the association with the nuclear activity is very unlikely. The only exception is NGC 6723-III60 (at $l = 0.^\circ02$, $b = -17.^\circ3$) that, with a distance of 7.5 ± 0.9 kpc, is close to Sgr A* and can potentially trace a Galactic wind. Excluding this single sightline would not alter our results.

Additionally, the bicone kinematics is incompatible with a nuclear wind. Even if the expanding bubble pushed gas at such large distances from Sgr A*, the $v_{\rm LSR}$ velocity of this material would be negative (approaching), and not positive (receding) as observed. In fact, the observed kinematics is well reproduced by a 'gentle' outflow with a vertical speed of ≈ 60 km s^{-1}, and not by the $\gtrsim 1000$ km s^{-1} wind that is needed reproduce the kinematics of the features observed within the Fermi Bubble (Bordoloi et al. 2017). Outflow velocities comparable with our estimate for v_z can be due to an expanding superbubble or to a particularly prominent star-forming region (e.g. Kim & Ostriker 2018). Unfortunately, pinpointing to the exact location in the disc where the ejection is supposed to occur is not straightforward and requires a dedicated dynamical investigation, which is currently ongoing (Li et al., in preparation).

6 CONCLUSIONS

The DHI of star-forming galaxies is thought to be composed of the combination of processed gas, expelled from the ISM in response to feedback processes from star formation and active galactic nuclei, and fresh material that accretes from the cosmic web. The characterization of the properties of this gas layer is a necessary step in the study of the gas cycle around galaxies, which in turn is key to understand galaxy evolution.

In Paper I, we have built a large data set of high- ($|v| > 90$ km s^{-1}) and intermediate-velocity ($40 < |v| < 90$ km s^{-1}) UV absorption features from the analysis of *HST* spectra of 55 Galactic halo stars with known distance measurements from the *Gaia* DR3 parallaxes. In this study (Paper II), we have determined the vertical distribution of the absorbing gas and modelled its kinematics by comparing the distributions of the observed features in the phase space (i.e. the v–distance space) with those predicted by a simple model of a thick disc with three free kinematical parameters, namely the gas

rotational, vertical, and radial velocities (v_ϕ, v_z, v_R). Our results can be summarized as follows.

(i) We have determined the characteristic scale heights h of the absorbing gas from the relation between the covering factor and $|z|$, finding $h = 1.4 \pm 0.2$ kpc for the whole data set and 1.0 ± 0.3 and 2.8 ± 0.3 kpc for the IVCs and HVCs, respectively (Section 2.1), in agreement with previous measurements.

(ii) At least two separate components are required to reproduce the data. A single-component model features multiple peaks in the parameter posteriors, suggesting the need of multiple components.

(iii) A double-component model where the HVCs and the IVCs are treated as separate populations, each with its own parameter set, provides only a partial description of the data as it fails to reproduce several features at $v_{LSR} > 0$ (Fig. 3).

(iv) The data are better described by a double-component model made by a combination of an inflow and an outflow, both characterized by rotation with $v_\phi \simeq v_\odot$ and vertical speeds of 50–100 km s^{-1} (Fig. 4).

(v) Most of the features associated with the outflow component are spatially confined towards two opposite directions in the sky, ($l = 220°$, $b = +40°$) and ($l = 40°$, $b = -40°$), indicating the presence of a biconic outflow driven by stellar feedback in the solar vicinity. The features associated with the inflow are instead spread more uniformly across the sky (Fig. 5).

Our results suggest that the classical, velocity-based separation between HVCs and IVCs is phenomenological as it is not associated with physically distinct kinematics for the two cloud populations. Instead, they support a scenario where both the HVCs and the IVCs are manifestations, at different velocities, of the same cycle of gas triggered by stellar feedback: that is, the GF. While our results refer specifically to the tenuous gas traced by UV absorption lines, which is the subject of this study, similar conclusions can be drawn from the dynamics of the extraplanar H I of our Galaxy (Marasco et al. 2012; Fraternali et al. 2015; Marasco & Fraternali 2017). These considerations further highlight the importance of kinematic and dynamical models as necessary tools to infer the properties of gaseous haloes. We caution that further work is required to robustly assess whether the differences in metallicity and dust content observed between the IVC and HVC populations are fully compatible with the mixing between the fountain clouds and the CGM proposed in the GF framework of Fraternali (2017).

A corollary of our findings – also applicable to studies of the DHI in external galaxies – is that if the ascending and descending phases of the GF are systematically characterized by different filling factors, the latter will be observed more frequently and consequently be considered as evidence for gas accretion on to the galaxy. When only a few sightlines per galaxy are observed, the outflow component may be missed completely, leading to an erroneous interpretation of the overall DHI kinematics.

We remark that the DHI models used in this study are deliberately simple, both in terms of structure (we assume a flat surface density profile) and kinematics (we use spatially constant velocity components). While this simplicity is necessary, given that more complex models are poorly constrained by our data (see Section 3.1), it also limits their physical accuracy. For instance, regardless of whether the DHI is produced by extragalactic infall or the fountain cycle, the vertical velocity is supposed to significantly vary with z due to the combined effects of gravity and hydrodynamical drag. The use of dynamical models (Fraternali & Binney 2006; Marasco et al. 2012; Afruni, Fraternali & Pezzulli 2021; Afruni, Pezzulli & Fraternali 2022) is a natural next step to improve on the present study.

ACKNOWLEDGEMENTS

The authors thank an anonymous referee for a detailed and constructive report. AM acknowledges the support by INAF/Frontiera through the 'Progetti Premiali' funding scheme of the Italian Ministry of Education, University, and Research. Support for this research was initially and partially provided by NASA through grant HST-GO-12982 from the Space Telescope Science Institute, which is operated by the Association of Universities for Research in Astronomy, Incorporated, under NASA contract NAS5-26555. Based on observations made with the NASA/ESA *Hubble Space Telescope*, obtained from the data archive at the Space Telescope Science Institute. STScI is operated by the Association of Universities for Research in Astronomy, Inc. under NASA contract NAS 5-26555. This work has made use of data from the European Space Agency (ESA) mission *Gaia* (https://www.cosmos.esa.int/gaia), processed by the *Gaia* Data Processing and Analysis Consortium (DPAC, https://www.cosmos.esa.int/web/gaia/dpac/consortium). Funding for the DPAC has been provided by national institutions, in particular the institutions participating in the *Gaia* Multilateral Agreement. This research was supported in part by the National Science Foundation under Grant No. NSF PHY-1748958.

DATA AVAILABILITY

The data underlying this paper are available in Paper I and in its online supplementary material.

REFERENCES

Afruni A., Fraternali F., Pezzulli G., 2021, MNRAS, 501, 5575
Afruni A., Pezzulli G., Fraternali F., 2022, MNRAS, 509, 4849
Armillotta L., Fraternali F., Werk J. K., Prochaska J. X., Marinacci F., 2017, MNRAS, 470, 114
Ben Bekhti N., Winkel B., Richter P., Kerp J., Klein U., Murphy M. T., 2012, A&A, 542, A110
Binney J., Nipoti C., Fraternali F., 2009, MNRAS, 397, 1804
Bish H. V., Werk J. K., Prochaska J. X., Rubin K. H. R., Zheng Y., O'Meara J. M., Deason A. J., 2019, ApJ, 882, 76
Bland-Hawthorn J., Veilleux S., Cecil G. N., Putman M. E., Gibson B. K., Maloney P. R., 1998, MNRAS, 299, 611
Bordoloi R. et al., 2017, ApJ, 834, 191
Bregman J. N., 1980, ApJ, 236, 577
Chiappini C., Matteucci F., Romano D., 2001, ApJ, 554, 1044
Clark S., Bordoloi R., Fox A. J., 2022, MNRAS, 512, 811
Collins J. A., Shull J. M., Giroux M. L., 2003, ApJ, 585, 336
Dekel A., Birnboim Y., 2006, MNRAS, 368, 2
Di Teodoro E. M., Fraternali F., 2014, A&A, 567, A68
Di Teodoro E. M., McClure-Griffiths N. M., Lockman F. J., Denbo S. R., Endsley R., Ford H. A., Harrington K., 2018, ApJ, 855, 33
Di Teodoro E. M., McClure-Griffiths N. M., Lockman F. J., Armillotta L., 2020, Nature, 584, 364
Fernández X., Joung M. R., Putman M. E., 2012, ApJ, 749, 181
Fiore F. et al., 2017, A&A, 601, A143
Foreman-Mackey D., Hogg D. W., Lang D., Goodman J., 2013, PASP, 125, 306
Fox A. J. et al., 2015, ApJ, 799, L7
Fox A. J. et al., 2016, ApJ, 816, L11
Fox A. J., Richter P., Ashley T., Heckman T. M., Lehner N., Werk J. K., Bordoloi R., Peeples M. S., 2019, ApJ, 884, 53
Fraternali F., 2017, in Fox A., Davé R., eds, Astrophysics and Space Science Library, Vol. 430, Gas Accretion on to Galaxies. Springer, Berlin, p. 323
Fraternali F., Binney J. J., 2006, MNRAS, 366, 449
Fraternali F., Binney J. J., 2008, MNRAS, 386, 935
Fraternali F., Tomassetti M., 2012, MNRAS, 426, 2166

Fraternali F., van Moorsel G., Sancisi R., Oosterloo T., 2002, AJ, 123, 3124
Fraternali F., Oosterloo T., Sancisi R., 2004, A&A, 424, 485
Fraternali F., Marasco A., Armillotta L., Marinacci F., 2015, MNRAS, 447, L70
French D. M. et al., 2021, ApJ, 923, 50
Gaia Collaboration et al., 2021, A&A, 649, A1
Galyardt J., Shelton R. L., 2016, ApJ, 816, L18
Gentile G. et al., 2013, A&A, 554, A125
Heald G. et al., 2011, A&A, 526, A118
Heitsch F., Putman M. E., 2009, ApJ, 698, 1485
Hodges-Kluck E. J., Miller M. J., Bregman J. N., 2016, ApJ, 822, 21
Kalberla P. M. W., Burton W. B., Hartmann D., Arnal E. M., Bajaja E., Morras R., Pöppel W. G. L., 2005, A&A, 440, 775
Kataoka J. et al., 2013, ApJ, 779, 57
Kereš D., Katz N., Weinberg D. H., Davé R., 2005, MNRAS, 363, 2
Kereš D., Katz N., Fardal M., Davé R., Weinberg D. H., 2009, MNRAS, 395, 160
Kim C.-G., Ostriker E. C., 2018, ApJ, 853, 173
Kooij R., Grønnow A., Fraternali F., 2021, MNRAS, 502, 1263
Lehner N., Howk J. C., 2010, ApJ, 709, L138
Lehner N., Howk J. C., 2011, Science, 334, 955
Lehner N., Prochaska J. X., Kobulnicky H. A., Cooksey K. L., Howk J. C., Williger G. M., Cales S. L., 2009, ApJ, 694, 734
Lehner N., Howk J. C., Thom C., Fox A. J., Tumlinson J., Tripp T. M., Meiring J. D., 2012, MNRAS, 424, 2896
Lehner N., Howk J. C., Marasco A., Fraternali F., 2022, MNRAS (Paper I)
Li A., Marasco A., Fraternali F., Trager S., Verheijen M. A. W., 2021, MNRAS, 504, 3013
Liang C. J., Chen H.-W., 2014, MNRAS, 445, 2061
Lockman F. J., Murphy E. M., Petty-Powell S., Urick V. J., 2002, ApJS, 140, 331
McClure-Griffiths N. M., Green J. A., Hill A. S., Lockman F. J., Dickey J. M., Gaensler B. M., Green A. J., 2013, ApJ, 770, L4
McMillan P. J., 2017, MNRAS, 465, 76
Marasco A., Fraternali F., 2011, A&A, 525, A134
Marasco A., Fraternali F., 2017, MNRAS, 464, L100
Marasco A., Fraternali F., Binney J. J., 2012, MNRAS, 419, 1107
Marasco A., Marinacci F., Fraternali F., 2013, MNRAS, 433, 1634
Marasco A. et al., 2019, A&A, 631, A50 (M19)
Marinacci F., Fraternali F., Nipoti C., Binney J., Ciotti L., Londrillo P., 2011, MNRAS, 415, 1534
Mitchell P. D., Schaye J., Bower R. G., 2020, MNRAS, 497, 4495
Muratov A. L., Kereš D., Faucher-Giguère C.-A., Hopkins P. F., Quataert E., Murray N., 2015, MNRAS, 454, 2691
Nipoti C., 2010, MNRAS, 406, 247
Olano C. A., 2008, A&A, 485, 457
Oosterloo T., Fraternali F., Sancisi R., 2007, AJ, 134, 1019
Pezzulli G., Fraternali F., 2016, MNRAS, 455, 2308
Pezzulli G., Fraternali F., Binney J., 2017, MNRAS, 467, 311
Ponti G. et al., 2019, Nature, 567, 347
Putman M. E., 2006, ApJ, 645, 1164
Qu Z., Bregman J. N., Hodges-Kluck E., Li J.-T., Lindley R., 2020, ApJ, 894, 142
Richter P., Sembach K. R., Wakker B. P., Savage B. D., Tripp T. M., Murphy E. M., Kalberla P. M. W., Jenkins E. B., 2001, ApJ, 559, 318
Richter P. et al., 2017, A&A, 607, A48
Rubin K. H. R., Prochaska J. X., Koo D. C., Phillips A. C., Martin C. L., Winstrom L. O., 2014, ApJ, 794, 156
Ryans R. S. I., Keenan F. P., Sembach K. R., Davies R. D., 1997a, MNRAS, 289, 83
Ryans R. S. I., Keenan F. P., Sembach K. R., Davies R. D., 1997b, MNRAS, 289, 986
Saintonge A. et al., 2013, ApJ, 778, 2
Sancisi R., Fraternali F., Oosterloo T., van der Hulst T., 2008, A&AR, 15, 189
Savage B. D., Sembach K. R., 1996, ARA&A, 34, 279
Schönrich R., McMillan P. J., 2017, MNRAS, 467, 1154
Sembach K. R. et al., 2003, ApJS, 146, 165
Shapiro P. R., Field G. B., 1976, ApJ, 205, 762
Shull J. M., Jones J. R., Danforth C. W., Collins J. A., 2009, ApJ, 699, 754
Smith G. P., 1963, Bull. Astron. Inst. Neth., 17, 203
Sobacchi E., Sormani M. C., 2019, MNRAS, 486, 205
Sormani M. C., Sobacchi E., 2019, MNRAS, 486, 215
Su M., Slatyer T. R., Finkbeiner D. P., 2010, ApJ, 724, 1044
Thom C., Putman M. E., Gibson B. K., Christlieb N., Flynn C., Beers T. C., Wilhelm R., Lee Y. S., 2006, ApJ, 638, L97
Thom C., Peek J. E. G., Putman M. E., Heiles C., Peek K. M. G., Wilhelm R., 2008, ApJ, 684, 364
Trapp C. W. et al., 2022, MNRAS, 509, 4149
Tripp T. M. et al., 2003, AJ, 125, 3122
Tumlinson J. et al., 2011, ApJ, 733, 111
van de Voort F., Springel V., Mandelker N., van den Bosch F. C., Pakmor R., 2019, MNRAS, 482, L85
Veilleux S., Cecil G., Bland-Hawthorn J., 2005, ARA&A, 43, 769
Wakker B. P., 1991, A&A, 250, 499
Wakker B. P., 2001, ApJS, 136, 463
Wakker B. P., 2004, in van Woerden H., Wakker B. P., Schwarz U. J., De Boer K. S., eds, Astrophysics and Space Science Library, Vol. 312, HVC/IVC Maps and HVC Distribution Functions. Kluwer, Dordrecht, p. 25
Wakker B. P., van Woerden H., 1997, ARA&A, 35, 217
Wakker B. P. et al., 2007, ApJ, 670, L113
Wakker B. P., York D. G., Wilhelm R., Barentine J. C., Richter P., Beers T. C., Ivezić Ž. , Howk J. C., 2008, ApJ, 672, 298
Werk J. K. et al., 2014, ApJ, 792, 8
Werk J. K. et al., 2016, ApJ, 833, 54
Werk J. K. et al., 2019, ApJ, 887, 89
Westmeier T., 2018, MNRAS, 474, 289
Zech W. F., Lehner N., Howk J. C., Dixon W. V. D., Brown T. M., 2008, ApJ, 679, 460
Zheng Y., Peek J. E. G., Werk J. K., Putman M. E., 2017, ApJ, 834, 179
Zheng Y. et al., 2020, ApJ, 896, 143

APPENDIX A: HVCS CAN CO-ROTATE WITH THE DISC

The $v_{\rm LSR}$ of a cloud rotating with velocity $v_\phi = v_\odot$ is given by (e.g. Wakker 2004, p. 27)

$$v_{\rm LSR} = v_\odot \left(\frac{R_\odot}{R} - 1 \right) \sin(l) \cos(b) \tag{A1}$$

thus it depends on its Galactocentric radius R. There are several instances where $|v_{\rm LSR}|$ can cross the 90–100 km s^{-1} threshold and enter the HVC regime. A simple case is when $R \gg R_\odot$ To illustrate this, in Fig. A1, we show the $v_{\rm LSR}$ maps predicted for three spherical shells of clouds, all centred at the Galactic Centre and rotating with $v_\phi = v_\odot$, but having radii of 10, 20, and 30 kpc (see below). More distant clouds show larger $|v_{\rm LSR}|$, as a reflection of the motion of the Sun. At $R > 10$ kpc, in several locations in the sky, a perfectly co-rotating cloud will appear as an HVC.

Clearly, the presence of additional velocity components can further increase the value of $|v_{\rm LSR}|$. For instance, vertical motions largely contribute to the LSR velocity at high $|b|$ (scaling as $v_z \sin(b)$), where the contribution of rotation is minimal. Lagging rotation, routinely observed in the DHI of external galaxies (e.g. Fraternali et al. 2004; Oosterloo et al. 2007; Gentile et al. 2013; Marasco et al. 2019), amplifies the effect shown in Fig. A1 causing closer clouds to appear as HVCs in some locations in the sky. The combined effect of rotation, vertical, and radial motions for a distribution of clouds with variable distance can produce very complex kinematic patterns that require a statistical approach to be applied to the data, like the one carried out in this study.

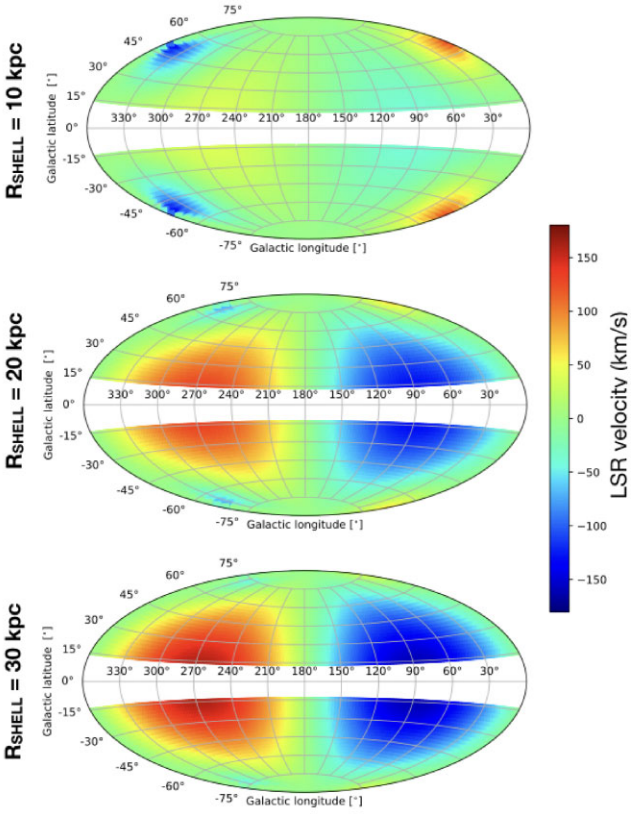

Figure A1. LSR–velocity maps for three infinitely thin shells of gas, all centred at the Galactic Centre and rotating with $v_\phi = v_\odot$. The shell radius is 10 kpc in the top panel, 20 kpc in the central panel, and 30 kpc in the bottom panel. More distant clouds can exhibit larger $|v_{\rm LSR}|$.

APPENDIX B: MODEL CORNER PLOTS

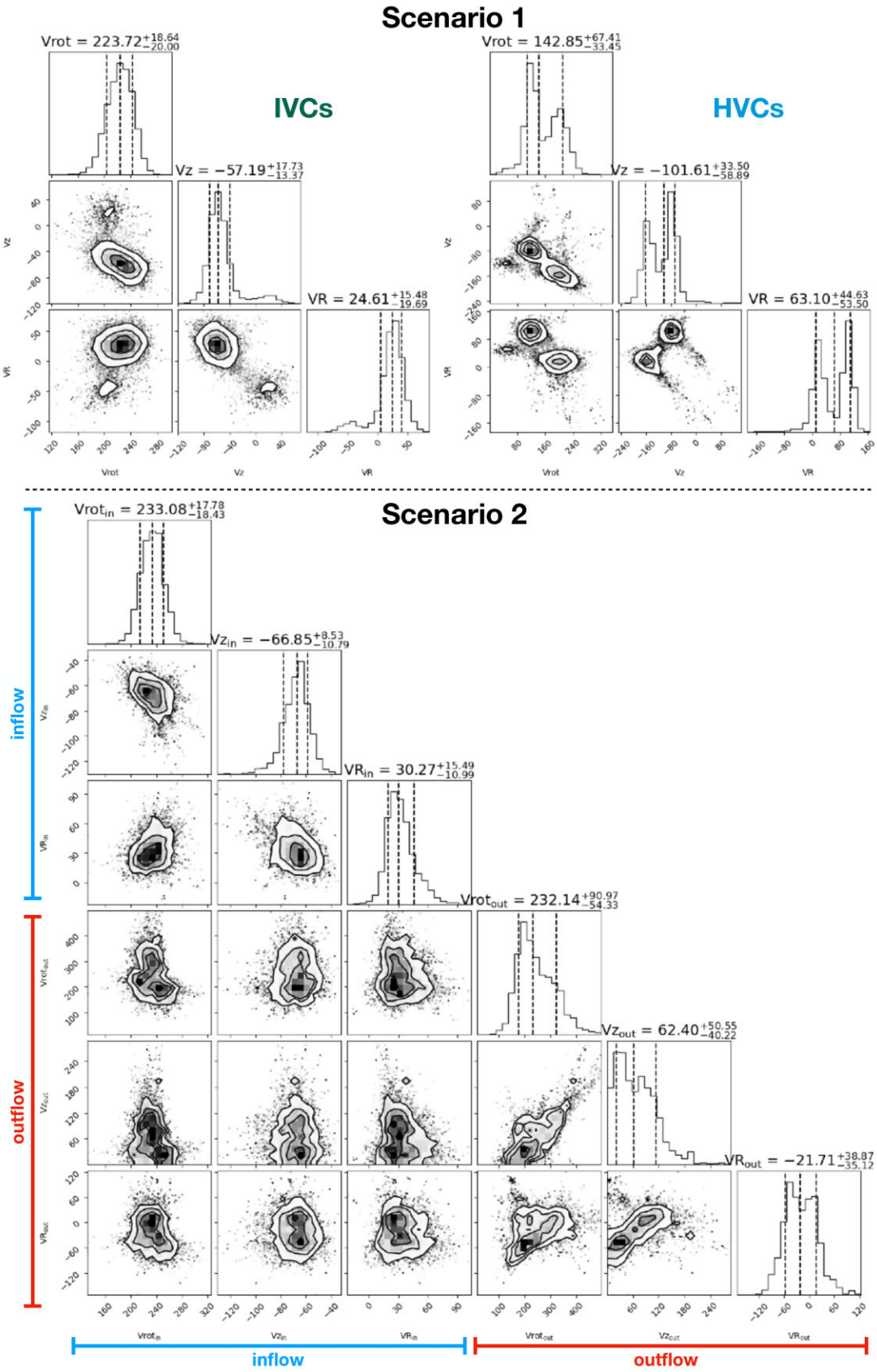

Figure B1. Corner plots showing the correlation between the various parameters used in our kinematic models of the Galactic DHI. The top panels refer to our IVC + HVC scenario (Section 4.1), and the bottom panels refer to our inflow + outflow scenario (Section 4.2).

This paper has been typeset from a TEX/LATEX file prepared by the author.